ACS OMEGA

http://pubs.acs.org/journal/acsodf

Article

Synthesis of Epitaxial MoS_2/MoO_2 Core–Shell Nanowires by Two-Step Chemical Vapor Deposition with Turbulent Flow and Their Physical Properties

Manami Goto, Ichiro Yamane, Shoki Arasawa, Takashi Yanase, Seiya Yokokura,* Taro Nagahama, Yu-lun Chueh, Yongjun Shin, Yongmin Kim, and Toshihiro Shimada*

Cite This: *ACS Omega* 2022, 7, 39362–39369

Read Online

ACCESS | Metrics & More | Article Recommendations | Supporting Information

ABSTRACT: MoO_2 nanowires (NWs), MoO_2/MoS_2 core–shell NWs, and MoS_2 nanotubes (NTs) were synthesized by the turbulent flow chemical vapor deposition of MoO_2 using MoO_3, followed by sulfurization in the sulfur gas flow. The involvement of MoO_x suboxide is suggested by density functional theory (DFT) calculations of the surface energies of MoO_2. The thickness of the MoS_2 layers can be controlled by precise tuning of sulfur vapor flow and temperatures. MoS_2 had an armchair-type winding topology due to the epitaxial relation with the MoO_2 NW surface. A single ~ few-layer MoO_2/MoS_2 core–shell structure showed photoluminescence after the treatment with a superacid. The resistivities of an individual MoO_2 NW and a MoS_2 NT were measured, and they showed metallic and semiconducting resistivity–temperature relationships, respectively.

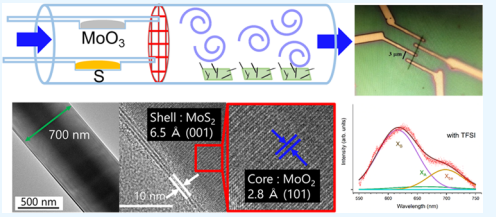

1. INTRODUCTION

One-dimensional nanomaterials (1D) have been synthesized from various atomic layer materials as nanotubes (NTs), such as carbon NTs (CNTs) from graphene[1] and inorganic NTs (INTs) from transition metal dichalcogenides.[2,3] They exhibit various functions due to their unique electronic structures arising from reduced dimensionality and symmetry. CNTs exhibit a distinct difference in their electronic structures depending upon the chirality of the winding patterns.[4] Similarly, different electronic structures in the INTs are predicted by theoretical calculations.[5−7] The scalable synthesis of the INTs is limited to MoX_2 and WX_2 (X = S, Se, Te) because Mo and W have volatile trioxides, which are essential to the formation of nanowires (NWs) of the suboxides that work as precursors of the INTs. INT formation has been reported using various methods such as the thermal reaction of metal oxide precursors with H_2S,[2,3,8] thermal decomposition of $(NH_3)_2MoS_4$,[9] chemical vapor transport (CVT),[10] CVT with C_{60},[11] the reaction in a nanoporous Al_2O_3 template,[12] heating of MoS_2 with a nucleation reagent (Mo,[13] SiO_2[14]), and chemical vapor deposition (CVD) methods with a flowing carrier gas.[8,15] We have reported the CVD synthesis of MoS_2 NTs using iron nanoparticles as catalysts.[16,17] However, the synthesis of MoS_2 NTs remains a major challenge in terms of NT purity, uniformity, and mass synthesis. A recent report[18] has solved the mystery of the poor yield of MoS_2 NTs without catalyst nanoparticles, in which the precursory suboxide NW was identified as less stable than the W counterparts. This is probably the reason why the study of the physical properties of the MoS_2 NTs is very limited compared to the WS_2 counterparts, which includes high current field effect transistors (FETs),[19] superconductivity,[20] intrinsic photovoltaic effects,[21] and second harmonic generation.[22] The applications of well-defined MoS_2 NTs in the literature are only FETs with limited mobility,[10,23] optical absorption with structural resonance,[24,25] and NO_2 sensors.[26] There are few photoluminescence studies on MoS_2 NT despite that it is a unique probe and important application of MoS_2 monolayers, which have a direct band gap, distinctly different from the indirect band gap of the bulk MoS_2.[27] Very recently, a PL of single-layer MoS_2NT was reported.[28]

In this paper, we report the scalable synthesis of MoO_2 NWs by turbulent flow CVD, sulfurization of MoO_2 NWs by elemental S to form the MoO_2/MoS_2 core–shell structures with various thicknesses, and measurement of their physical properties, including the resistivity of the MoO_2 NWs and MoS_2 NTs and PL of the MoO_2/MoS_2 core–shell structures. A distinct difference from previous reports in terms of the synthesis is in not using toxic H_2S as the sulfur source and the use of the two-step reaction—formation of MoO_2 NWs and sulfurization for the thickness control of the MoS_2 shells. The surface energies of MoO_2 were calculated by density functional theory (DFT) to examine the involvement of the suboxides in the formation of the MoO_2 NWs.

Received: August 30, 2022
Accepted: October 5, 2022
Published: October 21, 2022

2. EXPERIMENTAL SECTION

2.1. CVD. A specially designed CVD apparatus was used to grow the MoO_2 and MoS_2 nanostructures, as shown in Figure 1: a three-zone tube furnace with a 28.6 mm diameter outer

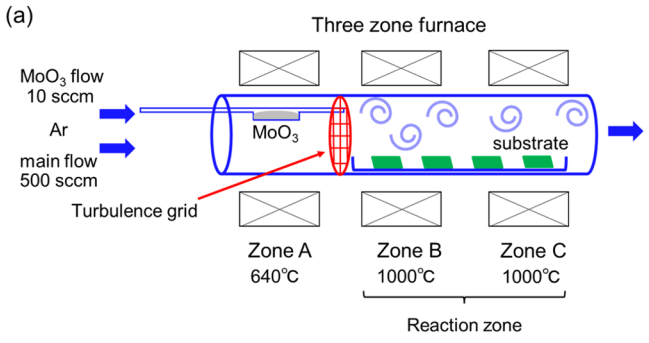

Figure 1. (a) Schematic illustration of CVD apparatus, (b) optical microscopy image of a stainless mesh, and (c) turbulence grid; the stainless mesh was inserted between the stainless holder.

quartz tube, two 4.0 mm diameter inner quartz tubes with MoO_3 and/or sulfur, respectively, and a turbulence grid. This tube furnace allows independent control of the temperatures of the material sublimation site (zone A) and the reaction sites (zones B and C). Ar was used as the carrier gas, and two flows were employed to independently control the raw material flow and the main flow. Al_2O_3 and Si wafers with thermal oxide films were placed in the reaction zones (zones B and C) as substrates for the nanostructure growth. The most distinctive feature of this CVD system is the turbulence grating inserted in the main flow. The turbulence grid consists of about 10 stainless meshes (wire diameter 0.1 mm with 0.15 mm opening) (see Figure 1b), which were placed in the stainless holder, as shown in Figure 1c. The turbulence grid has been used in hydrodynamics to produce turbulence flow, which can effectively change the morphology of the products in CVD.[8,29] Turbulence flow is supposed to enhance the nucleation in the carrier gas because turbulence increases the collision rate of molecules to the substrate and produces enough energy for nucleation as a result.

After optimizing the conditions of the temperature, flow rate, and reaction time, the following condition was adopted for the MoO_2 NWs with a high aspect ratio. After setting the source material and substrates, the CVD system was thoroughly evacuated by a rotary pump. After the air was purged to around 5 Pa, the system was filled with Ar gas. The CVD experiment was then performed at atmospheric pressure. The temperatures of the MoO_3 source (zone A) and reaction zone (zones B and C) were ramped from room temperature to 640 and 1000 °C, respectively, for 2.5 h. During this ramping period, there was no carrier gas flow through the MoO_3 source, while that of the main flow was 100 sccm. After the designed temperatures were reached, the flow rate through the MoO_3 source and the main flow was set to 10 and 500 sccm, respectively, for 2 h. The furnace was then naturally cooled to room temperature, and the carrier gas flow rates of MoO_3 and main flow were reduced to 0 and 100 sccm, respectively. As a result, the MoO_2 NWs were obtained. Next, to obtain MoS_2 NT, the sulfurization of the MoO_2 NWs was performed by setting the reaction temperature in zones B and C to 400−900 °C and the sulfur source temperature in the other furnace at 260 °C, with the duration time as a variable parameter.

MoO_3 (Kanto Chemical, >99.5%) and S (Kanto Chemical, >99.5%) powders were utilized as the source materials without further purification. Al_2O_3 (5 × 5 mm^2) (*c*-plane) and 1 × 1 cm^2 SiO_2 (285 nm)/Si wafers were used as the substrates. The substrates were cleaned by the RCA (Radio Corporation of America) cleaning method[30] to remove any metal and organic contaminants. Sapphire was annealed in the air for 1 h at 1000 °C to obtain a surface with atomic steps.[31]

2.2. Characterization. The products were characterized by an optical microscope, a SEM (JEOL JSM-6500F), Raman spectroscopy (Renishaw Invia with 532 nm excitation), and XPS (JEOL JPS-9200). The morphology and crystal orientations of the NWs were determined by a TEM (JEOL JEM-2010, 200 kV). Atomic-resolution images were obtained by an aberration-correction TEM (FEI Titan 300). Cross-section samples of the NWs were prepared by FIB-SEM (JEOL JSEM-6500F). For the Raman and TEM measurements, we selected one NW from the original substrate and put it on a fresh SiO_2/Si substrate using a Micro Pickup System (MicroSupport Axis Pro) to remove possible molybdenum compound peaks not from the NW on the original substrate.

To fabricate electrical contacts for the transport measurements, we prepared the samples as follows: the samples were dispersed in ethanol and drop-coated on SiO_2/Si (semi-insulating, resistivity > 1 MΩ cm^{-1}) substrates. Poly(methyl methacrylate) (PMMA) on the substrates was used as an electron-beam (e-beam) resist. The 50-nm-thick gold electrical contacts were then fabricated by e-beam lithography and thermal evaporation techniques. The electrical resistance was measured using the standard four-point probe lock-in method, while the sample temperature was controlled from 300 to 2 K in a variable temperature insert, which was immersed in a liquid ^{4}He bath.

2.3. DFT Calculations. DFT calculations were employed to estimate the surface energies of the various faces of a MoO_2 crystal to understand the growth mechanism of the MoO_2 NWs. We used the Vienna ab initio simulation package (VASP),[32] which uses plane wave basis functions and pseudopotential with projector augmented waves (PAW). The Perdew−Burke−Ernzerhof (PBE) functional,[33] the 8 × 8 × 1 *k*-point mesh, and a cutoff energy of 700 eV were used to calculate the (110), (011), (11$\bar{1}$), ($\bar{1}$11), (101), and (010) faces of the *P*21/*n* symmetry MoO_2. A slab model was used, in which a >10 Å thick vacuum was inserted between the slab, and two atomic layers near the surface were optimized. The surface energies σ were obtained as

$$\sigma = \frac{1}{A}(E_{slab} - nE_{bulk})$$

where A, n, E_{bulk}, and E_{slab} are the surface area of the slab, number of atoms in the slab, energy of the bulk, and energy of the slab, respectively.

https://doi.org/10.1021/acsomega.2c05586
ACS Omega 2022, 7, 39362−39369

3. RESULTS AND DISCUSSION

3.1. MoO_2 NWs. The MoO_2 NWs were selectively obtained by CVD with turbulence grating. MoO_3 was sublimated by heating to 640 °C, and then transported to the reaction site at 1000 °C by Ar gas, an inert gas, where it was reduced from MoO_3 to MoO_2 to earn entropy. The NWs typically had the dimensions of a 150 nm diameter and a 40 μm length (Figure 2a). Comparing the dimensions of the obtained NWs with

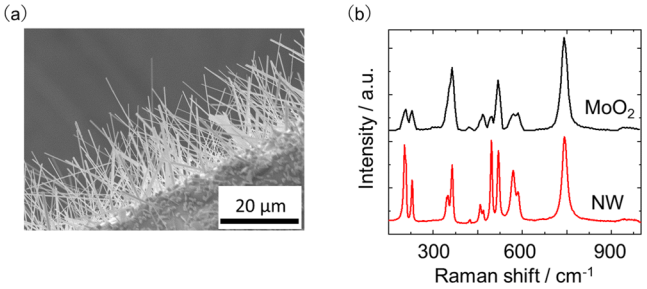

Figure 2. (a) FE-SEM image of MoO_2 NWs and (b) Raman spectra of the MoO_2 thick film (black) and single MoO_2 NW (red).

those previously reported, although the diameter of the obtained NWs is larger, the length is so long that an unprecedented high aspect ratio of up to 270 was achieved. In contrast, the CVD without turbulence grating yielded only plate-like MoO_2 crystals, suggesting that turbulence grating is a powerful tool for controlling the morphology of the CVD products. The density of the MoO_2 NWs was higher at the edge of the substrate, indicating that local turbulence at the edge could also help to synthesize the NWs. The Raman spectra (Figure 2b) of the NWs were in good agreement with those of the reported bulk MoO_2 crystals,[34] demonstrating the formation of MoO_2 NWs by this method.

The MoO_2 NWs were structurally characterized by TEM and selected area electron diffraction (SAED) measurements. The SAED pattern, obtained from the NW (Figure 3a,b), confirms the monoclinic MoO_2 phase and is consistent with previous reports.[35,36] The spot spacing of the diffraction pattern along the NW growth direction was 2.8 Å, which corresponds to the (101) plane spacing of MoO_2 with space group $P21/n$. The spot spacing perpendicular to the growth direction was 3.4 Å in Figure 3b. The TEM image and the SAED diffraction pattern of a cross section of the MoO_2 NW are shown in Figure 3c,d. The SAED diffraction pattern of the cross section shows a face spacing of 3.4 Å along the crystal facets, suggesting that the NWs were surrounded by $(\bar{1}11)$ or $(11\bar{1})$. It should be noted that MoO_2 has a unit cell similar to a hexagonal lattice ($\beta \approx 120$°, $a \approx c$), and the a:b ratio is special to give various orthogonal indices in the reciprocal space, including [101], $[\bar{1}11]$, and $[11\bar{1}]$ and [101], $[\bar{1}01]$, and [010].

To examine the growth mechanism of the MoO_2 NWs, the surface energies of the various faces were calculated using DFT of the slab models. Table 1 summarizes the result. The details of the calculation and the optimized surface structures are explained in the Supporting Information, including Figure S1. Since a crystal face tends to grow larger when the surface energy is lower, we expected that the surface energy of (101), which is the cross section of the NW, would be high and the surface energies of $(\bar{1}11)$ and $(11\bar{1})$, which form the sides of the NW, would be low. Table 1 does not show this tendency,

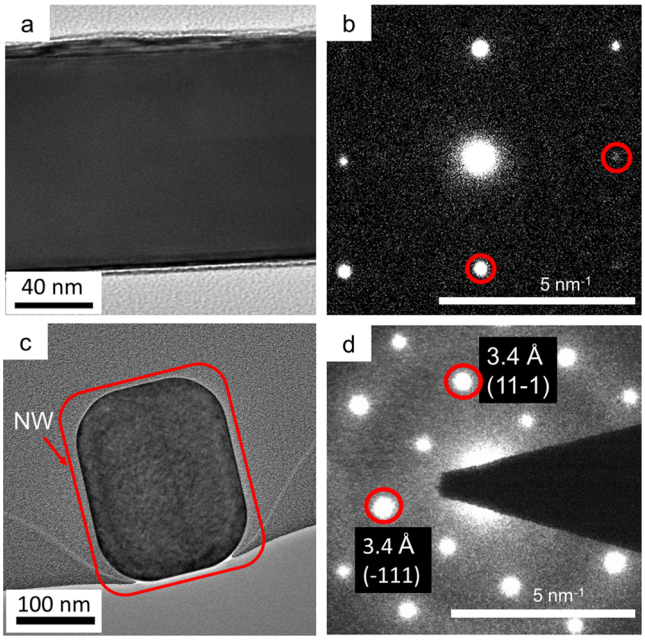

Figure 3. $P21/n$ MoO_2 NW characterization: TEM and SAED images of (a, b) side view and (c, d) cross-sectional view of MoO_2 NW.

resulting in a discrepancy between the calculated and experimental results. Therefore, it is considered that the 1D NW structure of MoO_2 was not formed based on thermodynamics governed by the surface energy. The feasible explanation is that the 1D NW structure was the result of the growth of excess oxide (such as the recently reported Mo_4O_{11}[18]), and it turned into MoO_2 NW. The temperature dependence of the resistivity, which will be discussed below, supports the existence of defects as expected from the stoichiometry conversion of the Mo oxides.

The electric conductivity of MoO_2 has not been measured on single crystalline samples, although the theoretical prediction[37] and measurement on polycrystalline films[38] were reported. Figure 4 shows the temperature dependence of the resistance of a MoO_2 NW measured in the temperature range from 300 to 2 K using the four-terminal method. In the temperature range from 300 to 50 K, the resistance showed a metallic temperature dependence, decreasing with decreasing temperature, whereas the resistance showed almost no temperature dependence in the temperature range below 50 K. This result is attributed to the dominance of thermal phonon scattering and impurity scattering at high and low temperatures, respectively. The metallic conduction behavior at high temperatures is consistent with theoretical calculations.[37] Ideally, the sample should show a metallic conduction behavior down to very low temperatures, but this sample probably contains impurities. In previous studies, it has been reported that the metallic electronic structure of MoO_2 is sensitive to its stoichiometry and lattice strain and that thin MoO_2 films show a thermally activated temperature dependence even at around room temperature.[38] Metallic conduction observed down to 50 K in the present study indicates that the MoO_2 NWs have excellent stoichiometry and alleviate strain.

It should be noted that the MoO_2 NW formation was greatly enhanced by introducing the turbulence grid and that the MoO_2 NWs are mostly found on the edge of the substrate (Figure 2a). This result shows that the nucleation of the NW precursor (such as Mo_4O_{11}) is strongly affected by the carrier

https://doi.org/10.1021/acsomega.2c05586
ACS Omega 2022, 7, 39362−39369

Table 1. Surface Energies of Various Faces of MoO_2

faces	(011)	(101)	(110)	($\bar{1}$11)	(11$\bar{1}$)	(010)	($\bar{1}$01)
surface energy/Jm^{-2}	2.25	1.84	2.36	2.55	2.55	1.30	1.75

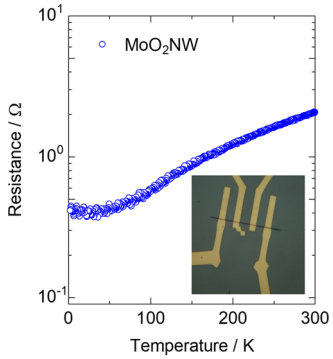

Figure 4. Temperature dependence of resistance measured for MoO_2 NW. The inset shows the image of the sample.

gas flow. The difficulty in the growth of the MoS_2 NTs in the previous reports probably comes from this strong influence of the hydrodynamic effects.

3.2. Formation of Armchair MoS_2 NT Shells from MoO_2 NWs. MoO_2/MoS_2 core−shell NTs were synthesized by a two-step CVD in which a sulfur stream was passed through the MoO_2 NW obtained by the above method. The conditions for the NT fabrication were optimized by fixing the sulfur heating temperature at 260 °C and the reaction time at 2 h and varying the reaction temperature from 400 to 1000 °C. In the Raman spectra of the NWs obtained at each reaction temperature (Figure 5), a peak characteristic of MoS_2 at

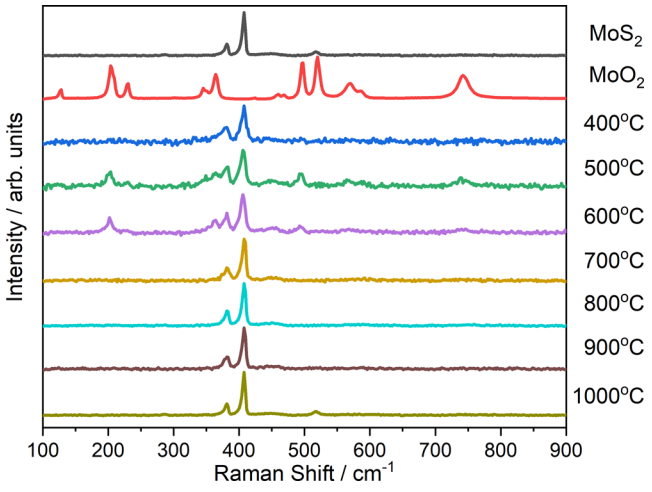

Figure 5. Raman spectra of a sulfur-annealed MoO_2 NW at each temperature. The data for the MoS_2 and MoO_2 thin films grown by CVD without turbulent flow are also shown as references.

around 382 cm^{-1}(E^1_{2g}) and 408 cm^{-1} (A_{1g}) was observed, suggesting the formation of MoS_2 at all reaction temperatures. In the Raman spectra of the products at temperatures below 600 °C, peaks derived from both MoS_2 and MoO_2 were observed, whereas only peaks derived from MoS_2 were observed for the products formed at higher temperatures above 600 °C. The region characteristic to MoO_x (600−900 cm^{-1}) only showed a 736 cm^{-1} peak corresponding to MoO_2[39] below 600 °C. The EDS spectrum also shows residual O below 600 °C (Supporting Information Figure S2), which is consistent with the Raman spectra. These results suggest the formation of NWs with a MoO_2-MoS_2 core−shell structure at lower temperatures and completely sulfurized MoS_2 NTs at higher temperatures. Nevertheless, we found that the sulfurization process is not only governed by the reaction temperature, time (2 h), and S source temperature, but other factors such as room temperature, relative humidity of the environment, and the time to dry the reaction system by flowing Ar gas. We suspect a great impact of residual water molecules in the reaction system on the sulfurization reaction. Currently, we cannot control these factors, and the degree of the reaction deviates among the experiments. In the following, we show the results after confirming the reaction degree by TEM observations.

The TEM and SAED results of the NW structure proved this prediction. In Supporting Information Figure S3, the TEM image of the NW produced at 400 °C is shown. A layer structure surrounding the NW was confirmed. A few layers of the MoS_2 layered structure are formed surrounding the MoO_2 NWs. In addition, the diffraction pattern of MoO_2-derived $P21/n$ was obtained in the SAED image, indicating that the crystal structure of the MoO_2 NW core is retained. Since MoO_2 is unlikely to evaporate at a reaction temperature of 400 °C, the formation of MoS_2NT would proceed via a solid-gas phase reaction, i.e., MoS_2 is epitaxially formed after S gas is adsorbed on the MoO_2 NW surface.

NWs formed at 700 °C showed both the MoO_2/MoS_2 core−shell structure and MoS_2 NT formation deviating among experimental batches. The HRTEM image of the MoO_2/MoS_2 core−shell structure formed at 700 °C is shown in Figure 6.

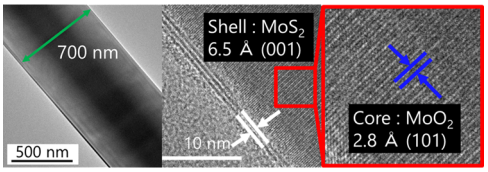

Figure 6. HRTEM image of the MoO_2/MoS_2 core−shell NW. The outer lattice distance of 6.5 Å corresponds to the MoS_2 (001) lattice distance. The inner lattice distance of 2.8 Å corresponds to the MoO_2 (101) lattice distance.

The HRTEM image shows two to three MoS_2 layers surrounding the MoO_2 NW. The lattice spacing of the inner and outer portions of the NW corresponds to MoO_2 (2.8 Å, (101)) and MoS_2 (6.5 Å, (001)), respectively.

The distribution of Mo, O, and S was examined by EDS (Supporting Infomation Figure S4). Mo was distributed throughout the structure, whereas O was mostly distributed in the center and S in the periphery. These results suggested the formation of a core−shell structure in which MoO_2 with a diameter of about 50 nm is covered by MoS_2 with a thickness of about 100 nm. The thicker MoS_2 in this sample compared to the core−shell structure formed at 400 °C suggests that the MoS_2 formation proceeds from the outside to the inside, using Mo oxide (in this case, MoO_2) as the raw material and the outer MoS_2 as a template. The synthesis at high temperatures

https://doi.org/10.1021/acsomega.2c05586
ACS Omega 2022, 7, 39362−39369

allows S to easily penetrate between the MoO_2 and MoS_2, which probably results in the effective formation of multilayers of MoS_2.

We found that all samples showed SAED patterns corresponding to the armchair chirality of the MoS_2. Figure 7 shows the TEM and SAED images of the MoO_2 /MoS_2

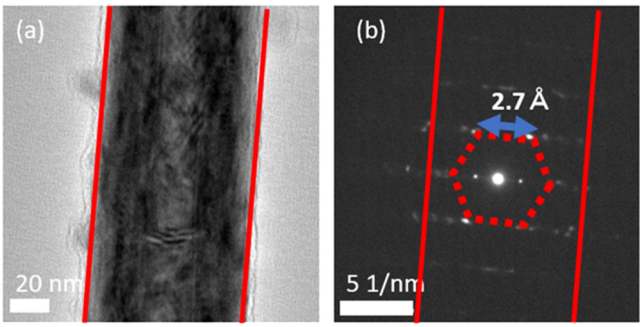

Figure 7. (a) TEM and (b) SAED image of a MoO_2/MoS_2 core -shell NW sulfurized at 700 °C.

core−shell NT formed at 700 °C. The diffraction from the core is very weak, and the pattern shows a sixfold symmetry originating from the honeycomb structure of MoS_2. The observed electron diffraction spot spacing (2.7 Å) is in good agreement with the value estimated from the lattice constant of the MoS_2 crystal (2.74 Å). Considering the relative relationship between the NT growth direction and the electron diffraction pattern, the MoS_2 NTs have an armchair-type chirality, as we have reported for the MoS_2 NTs by FeO-catalyzed growth.

As for the mechanism of formation of the armchair-type NTs, we considered the epitaxial relationship between the MoO_2 NW surface and MoS_2 essential. MoO_2 has a pseudo-hexagonal lattice (a_{MoO_2} = 5.55 Å $\simeq c_{MoO_2}$ = 5.62 Å and β = 119.69 $\simeq$ 120°). The lattice matching of $(a + c)/2$ (one lattice constant of (101) surface) and a_{MoS_2} = 3.16 Å is +2%. Although the length of b_{MoO_2} does not match with the lattice constant of MoS_2, this one-dimensional matching will stabilize the interface more than a mismatch in two directions in the van der Waals epitaxy.[40−42] There are some reports regarding the MoS_2 NTs or MoO_2/MoS_2 core−shell structures (including nanoplates or nanoclusters) showing electron diffraction patterns.[13,43,44] Various chiralities and orientations were reported, including zigzag,[13] armchair,[17] random,[43] and vertical alignment of the MoS_2 layers on MoO_2(110).[43] We consider that there are several reasons for the observations of armchair chirality in the present result. One is that the wide faces of the MoO_2 NWs are suitable for the planar growth of the MoS_2 layers, and van der Waals epitaxy comes into play. Another is that our experiment employs well-defined MoO_2 NWs prepared during the first step and very gentle sulfurization conditions with precautions to obtain reproducibility of the MoS_2 thickness as much as possible.

3.3. Structure and Stoichiometry of MoS_2 NTs after Complete Sulfurization. The cross-sectional TEM of MoS_2 NT formed at 700 °C is shown in Figure 8, where a cavity-like structure was observed; the EDS results confirmed the formation of the MoS_2NT with a hollow center, as no Mo, O, or S atoms were distributed in that region. Based on the HRTEM results, the face spacing of the formed MoS_2 layered

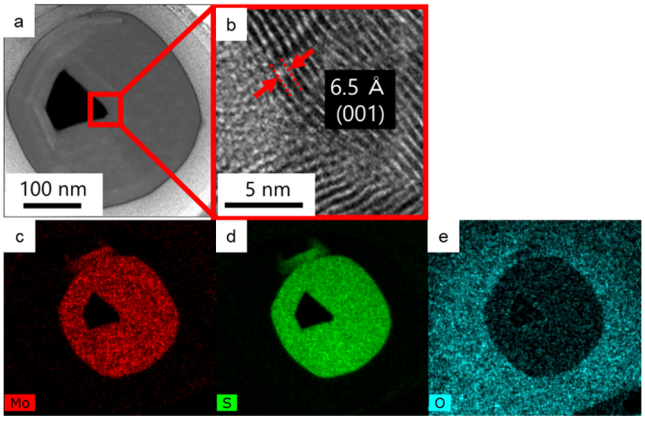

Figure 8. (a) Cross-sectional TEM image of a MoS_2 NT. (b) HRTEM image neat the center of the tube. (c−e) EDS mapping corresponding to Mo, S, and O.

structure was estimated to be 6.5 Å. This value is somewhat wider than the interlayer distance (face spacing (001)) of the bulk MoS_2 crystal (6.2 Å). We do not know the reason for this discrepancy, and the possible models include the strain of the folded layers and the adventitious intercalation of S or O atoms between the layers. A boundary structure with a different layer orientation was formed in the NT. The boundary line is formed toward the center of the NT, suggesting that the multilayered tube structure of MoS_2 progresses inward from the outer periphery. The volumes per Mo atom are 32.86 and 52.85 $Å^3$ for MoO_2 and MoS_2, respectively. This increased volume will pull out the materials and make the center void of MoS_2 NT. The stoichiometry of the aggregated MoS_2 NTs was evaluated by XPS (Figure S5 and Table S1 in the Supporting Information). By integrating the peaks and dividing them by the sensitivity factors, Mo:S = 1:1.83, indicating a sulfur deficiency.

At higher temperatures (800−1000 °C), the sulfurization reaction was complete. It was observed that a MoS_2NT was surrounded by SiO_x, which probably came from the quartz reaction tube (Figure S6 in the Supporting Information). The chirality of the MoS_2 NTs was armchair.

3.4. Photoluminescence. It is expected that the low temperature and short reaction time enables the synthesis of the MoO_2 core−monolayer MoS_2 shell structures. Since the photoluminescence of MoS_2 is an indication of a monolayer or a few-layer thickness, we examined the photoluminescence of the samples fabricated under various sulfurization conditions. It was difficult to make MoS_2 layers thin enough for this purpose at a temperature equal to or higher than 700 °C. It was reported that the photoluminescence of the monolayer MoS_2 is significantly weakened by electron doping, and it can be improved by depriving excess electrons by the treatment with superacid such as bis(trifluoromethanesulfonyl)imide (or trifluorosulfuric imide, TFSI, $C_2HF_6NO_4S_2$).[45] Figure 9 shows the photoluminescence from the NW sample sulfurized at 600 °C. Before the TFSI treatment, no PL was observed. After the TFSI treatment (drop casting 0.02 M TFSI in 1,2-dichloroethane in an Ar glovebox and dried), a strong PL signal was observed. By peak decomposition by least-squares fitting, the peak areas of the PL A-exciton (X_A, 663 nm):B-exciton (X_B, 618 nm):trion (678 nm):bound exciton due to a defect site (X_{be}, 698nm) = 5:74:0:21. The negligible intensity of the trion peak is consistent with previous reports on the superacid

https://doi.org/10.1021/acsomega.2c05586
ACS Omega 2022, 7, 39362−39369

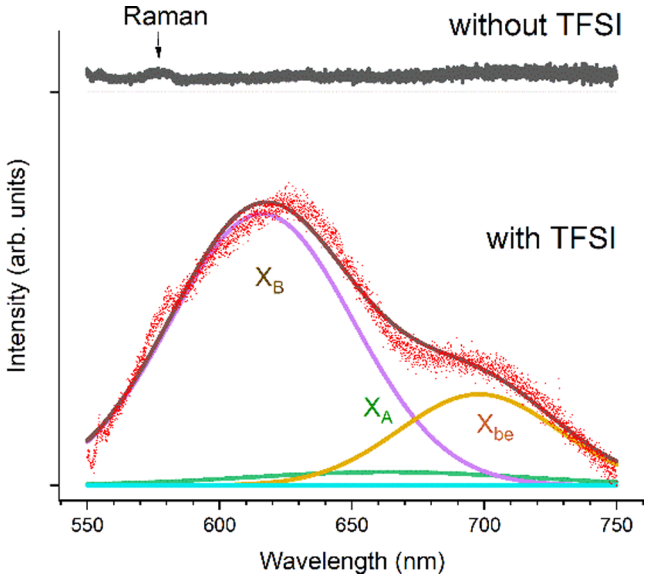

Figure 9. Photoluminescence of the MoO_2/MoS_2 core−shell sample sulfurized at 600 °C. After drop-coating TFSI, the sample showed photoluminescence. Curves X_A, X_B, and X_{be}, which were obtained by a least-squares fitting of the Gaussian peaks, denote A-exciton, B-exciton, and bound exciton, respectively. No trion peak was observed in the curve fitting result. Excitation was at 532 nm. The peaks observed around 580 nm are the Raman signal from MoS_2 with a 532 nm excitation

treatment of monolayer MoS_2, which eliminates the trion peak and increases the total photoluminescence intensity. Therefore, it is proved that the "MoO_2 core"—"a monolayer ∼ a few-layer MoS_2 shell" structure was successfully fabricated by the present method, although defect sites (X_{be}) and PL-quenching electron doping existed without the TFSI treatment.

3.5. Conductivity Measurement. The temperature dependence of the resistance of a MoS_2 NW fully sulfurized at 900 °C was measured in the temperature range from 300 to 2 K by the four-terminal method (Figure 10). The NW sample

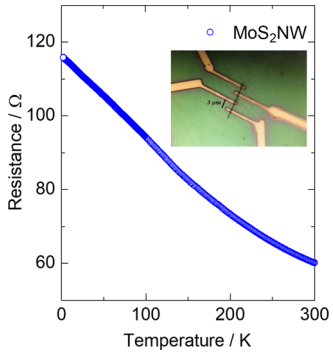

Figure 10. Temperature dependence of resistance measured for MoS_2 NT. The inset shows an image of the sample.

was covered by a single crystalline BN sheet to prevent contamination after the contact fabrication. In the temperature range from 300 to 200 K, the resistance exponentially increased, typical semiconducting behavior, whereas below 200 K, the resistance increased almost linearly with the temperature. The apparent temperature dependence of the resistance is thought to be reduced due to carrier doping caused by the S defects. The previous reports regarding MoS_2 NT FETs showed limited carrier mobilities ($<10^{-1}$ cm^2 V^{-1} s^{-1})[23] when grown by sulfurization of the MoO_x, whereas rather high mobilities (∼40 cm^2 V^{-1} s^{-1}) were observed when grown by CVT.[46] Reducing the defect concentration is an issue to be addressed in the future for high-performance semiconductor MoS_2NTs.

4. CONCLUSIONS

The MoO_2 NWs, MoO_2/MoS_2 core−shell NWs, and MoS_2 NTs were synthesized by turbulent flow chemical vapor deposition of MoO_2 using MoO_3 followed by sulfurization in sulfur gas flow. The involvement of MoO_x suboxide is suggested by DFT calculations of the surface energies of MoO_2. The thickness of the MoS_2 layers can be controlled by the precise control of the sulfur vapor flow and temperatures. MoS_2 had an armchair-type winding topology due to the epitaxial relation with the MoO_2 NW surface. A single ∼ few-layer MoO_2/MoS_2 core−shell structure showed photoluminescence after treatment with a superacid. The resistivities of an individual MoO_2 NW and a MoS_2 NT were measured and showed metallic and semiconducting resistivity−temperature relationships, respectively. The cross section of a MoS_2 NT showed a noncylindrical layer orientation, which might be responsible for the poor performance of the reported MoS_2 FETs. The improvement of the process parameters for the ideal structures will open the way for the quantum-mechanical properties arising from the NT structures.

■ ASSOCIATED CONTENT

Supporting Information

The Supporting Information is available free of charge at https://pubs.acs.org/doi/10.1021/acsomega.2c05586.

Optimized surface structure; EDS spectrum; EDS mapping; and XPS, TEM, and SAED measurements (PDF)

■ AUTHOR INFORMATION

Corresponding Authors

Seiya Yokokura − *Graduate School of Chemical Sciences and Engineering, Hokkaido University, Sapporo 060-8628, Japan; Division of Applied Chemistry, Faculty of Engineering, Hokkaido University, Sapporo 060-8628, Japan;* orcid.org/0000-0002-2671-8323; Email: seiyayokokura@eng.hokudai.ac.jp

Toshihiro Shimada − *Graduate School of Chemical Sciences and Engineering, Hokkaido University, Sapporo 060-8628, Japan; Division of Applied Chemistry, Faculty of Engineering, Hokkaido University, Sapporo 060-8628, Japan;* orcid.org/0000-0001-5122-1063; Email: shimadat@eng.hokudai.ac.jp

Authors

Manami Goto − *Graduate School of Chemical Sciences and Engineering, Hokkaido University, Sapporo 060-8628, Japan*

Ichiro Yamane − *Graduate School of Chemical Sciences and Engineering, Hokkaido University, Sapporo 060-8628, Japan*

Shoki Arasawa − *Graduate School of Chemical Sciences and Engineering, Hokkaido University, Sapporo 060-8628, Japan*

Takashi Yanase − *Department of Chemistry, Toho University, Funabashi 274-8510, Japan; Division of Applied Chemistry, Faculty of Engineering, Hokkaido University, Sapporo 060-8628, Japan;* orcid.org/0000-0002-5625-9308

https://doi.org/10.1021/acsomega.2c05586
ACS Omega 2022, 7, 39362−39369

Taro Nagahama − *Graduate School of Chemical Sciences and Engineering, Hokkaido University, Sapporo 060-8628, Japan; Division of Applied Chemistry, Faculty of Engineering, Hokkaido University, Sapporo 060-8628, Japan*
Yu-lun Chueh − *Department of Materials Science and Engineering, National Tsing Hua University, Hsinchu 300044, Taiwan R.O.C.;* orcid.org/0000-0002-0155-9987
Yongjun Shin − *Department of Materials Science and Engineering, Seoul National University, Seoul 08826, Korea;* orcid.org/0000-0001-9977-891X
Yongmin Kim − *Department of Physics, Dankook University, Cheonan 31116 Chungcheongnam-do, Korea;* orcid.org/0000-0001-9274-723X

Complete contact information is available at: https://pubs.acs.org/10.1021/acsomega.2c05586

Author Contributions

M.G. performed the growth and structural characterization of the samples (TEM, Raman) and wrote the first draft of this paper. I.Y. performed the DFT calculations. S.A. contributed to the photoluminescence measurement and data analysis. Y.S. and Y.K. performed the electrical measurement of the single NWs and NTs. Y.-L.C. contributed to the STEM characterization of the core−shell structures. T.Y. and T.S. designed present research and S.Y., T.Y., T.N., and T.S. prepared the manuscript.

Notes

The authors declare no competing financial interest.

■ ACKNOWLEDGMENTS

Instrumental analyses were supported by the Nanotechnology platform at Hokkaido University by the METI, Japan. The authors would like to thank Dr. Takashi Endo and Mr. Ryo Ota for the FIB and STEM operation. The computations in this work were done using the facilities of the Supercomputer Center, the Institute for Solid State Physics, the University of Tokyo under the project codes 2021-Ba-0028 and 2022-Ba-0061. This work was supported by the Foundation of Public Interest of Tatematsu and Iketani Science and Technology Foundation. The work at DKU was supported by the National Research Foundation of Korea (NRF-2016R1D1A1B01006437) funded by the Korea government (MSIT).

■ REFERENCES

(1) Iijima, S.; Ichihashi, T. Single-shell carbon nanotubes of 1-nm diameter. *Nature* **1991**, *354*, 56−58.
(2) Tenne, R.; Margulis, L.; Genut, M.; Hodes, G. Polyhedral and cylindrical structures of tungsten disulfide. *Nature* **1992**, *360*, 444−446.
(3) Margulis, L.; Salitra, G.; Tenne, R.; Talianker, M. Nested Fullerene-like Structrures. *Nature* **1993**, *365*, 113−114.
(4) Odom, T. W.; Huang, J. L.; Kim, P.; Lieber, C. M. Structure and electronic properties of carbon nanotubes. *J. Phys. Chem. B* **2000**, *104*, 2794−2809.
(5) Seifert, G.; Terrones, H.; Terrones, M.; Jungnickel, G.; Frauenheim, T. Structure and electronic properties of MoS_2 nanotubes. *Phys. Rev. Lett.* **2000**, *85*, 146−149.
(6) Li, N.; Lee, G.; Jeong, Y. H.; Kim, K. S. Tailoring Electronic and Magnetic Properties of MoS_2 Nanotubes. *J. Phys. Chem. C* **2015**, *119*, 6405−6413.
(7) Zhang, M.-Q.; Weng, M.-T.; Tamura, T.; Goto, M.; Yamane, I.; Yanase, T.; Nagahama, T.; Shimada, T. DFT calculation of square MoS_2 nanotubes. *Phys. E* **2021**, *130*, No. 114693.
(8) Feldman, Y.; Wasserman, E.; Srolovitz, D. J.; Tenne, R. High-rate, gas-phase growth of MoS_2 nested inorganic fullerenes and nanotubes. *Science* **1995**, *267*, 222−225.
(9) Nath, M.; Govindaraj, A.; Rao, C. N. R. Simple synthesis of MoS_2 and WS_2 nanotubes. *Adv. Mater.* **2001**, *13*, 283−286.
(10) Remskar, M.; Skraba, Z.; Cleton, F.; Sanjines, R.; Levy, F. MoS_2 as microtubes. *Appl. Phys. Lett.* **1996**, *69*, 351−353.
(11) Remskar, M.; Mrzel, A.; Skraba, Z.; Josih, A.; Ceh, M.; Demsar, J.; Stadelmann, P.; Levy, F.; Mihailovic, D. Self-Assembly of Subnanometer-Diameter Single-Wall MoS_2 Nanotubes. *Science* **2001**, *292*, 479−481.
(12) Zelenski, C. M.; Dorhout, P. K. Template synthesis of near-monodisperse microscale nanofibers and nanotubules of MoS_2. *J. Am. Chem. Soc.* **1998**, *120*, 734−742.
(13) Hsu, W. K.; Chang, B. H.; Zhu, Y. Q.; Han, W. Q.; Terrones, H.; Terrones, M.; Grobert, N.; Cheetham, A. K.; Kroto, H. W.; Walton, D. R. An Alternative Route to Molybdenum Disulfide Nanotubes. *J. Am. Chem. Soc.* **2000**, *122*, 10155−10158.
(14) Gordon, J. M.; Katz, E. A.; Feuermann, D.; Albu-Yaron, A.; Levy, M.; Tenne, R. Singular MoS2, SiO2 and Si Nanostructures - Synthesis by Solar Ablation. *J. Mater. Chem.* **2008**, *18*, 458−462.
(15) Feldman, Y.; Wasserman, E.; Srolovitz, D.; Tenne, R. High-Rate, Gas-Phase Growth of MoS_2 Nested Inorganic Fullerenes and Nanotubes. *Science* **1995**, *267*, 222−225.
(16) Mengting, W.; Yanase, T.; Uehara, F.; Watanabe, S.; Miura, T.; Nagahama, T.; Shimada, T. Switching of the products by changing the size and shape of catalytic nanoparticles during CVD growth of MoS_2 nanotubes. *CrystEngComm* **2017**, *19*, 3915−3920.
(17) Weng, M. T.; Zhang, M.-Q.; Yanase, T.; Uehara, F.; Nagahama, T.; Shimada, T. Catalytic chemical vapor deposition and structural analysis of MoS_2 nanotubes. *Jpn. J. Appl. Phys.* **2018**, *57*, No. 030304.
(18) Chithaiah, P.; Ghosh, S.; Idelevich, A.; Rovinsky, L.; Livneh, T.; Zak, A. Solving the "MoS_2 Nanotubes" Synthetic Enigma and Elucidating the Route for Their Catalyst-Free and Scalable Production. *ACS Nano* **2020**, *14*, 3004−3016.
(19) Levi, R.; Bitton, O.; Leitus, G.; Tenne, R.; Joselevich, E. Field-effect transistors based on WS_2 nanotubes with high current-carrying capacity. *Nano Lett.* **2013**, *13*, 3736−3741.
(20) Qin, F.; Ideue, T.; Shi, W.; Zhang, X. X.; Yoshida, M.; Zak, A.; Tenne, R.; Kikitsu, T.; Inoue, D.; Hashizume, D.; Iwasa, Y. Diameter-Dependent Superconductivity in Individual WS_2 Nanotubes. *Nano Lett.* **2018**, *18*, 6789−6794.
(21) Zhang, Y. J.; Ideue, T.; Onga, M.; Qin, F.; Suzuki, R.; Zak, A.; Tenne, R.; Smet, J. H.; Iwasa, Y. Enhanced intrinsic photovoltaic effect in tungsten disulfide nanotubes. *Nature* **2019**, *570*, 349−353.
(22) Xia, H.; Chen, X.; Luo, S.; Qin, F.; Idelevich, A.; Ghosh, S.; Ideue, T.; Iwasa, Y.; Zak, A.; Tenne, R.; Chen, Z.; Liu, W.-T.; Wu, S. Probing the Chiral Domains and Excitonic States in Individual WS2 Tubes by Second-Harmonic Generation. *Nano Lett.* **2021**, *21*, 4937−4943.
(23) Strojnik, M.; Kovic, A.; Mrzel, A.; Buh, J.; Strle, J.; Mihailovic, D. MoS_2 nanotube field effect transistors. *AIP Adv.* **2014**, *4*, No. 097114.
(24) Kazanov, D. R.; Poshakinskiy, A. V.; Davydov, V.; Smirnov, A. N.; Eliseyev, I. A.; Kirilenko, D. A.; Remskar, M.; Fathipour, S.; Mintairov, A.; Seabaugh, A.; Gil, B.; Shubina, T. V. Multiwall MoS_2 tubes as optical resonators. *Appl. Phys. Lett.* **2018**, *113*, No. 101106.
(25) Sinha, S. S.; Yadgarov, L.; Aliev, S. B.; Feldman, Y.; Pinkas, I.; Chithaiah, P.; Ghosh, S.; Idelevich, A.; Zak, A.; Tenne, R. MoS_2 and WS_2 Nanotubes: Synthesis, Structural Elucidation, and Optical Characterization. *J. Phys. Chem. C* **2021**, *125*, 6324−6340.
(26) Kumar, R.; Goel, N.; Kumar, M. High performance NO_2 sensor using MoS_2 nanowires network. *Appl. Phys. Lett.* **2018**, *112*, No. 053502.

(27) Splendiani, A.; Sun, L.; Zhang, Y.; Li, T.; Kim, J.; Chim, C. Y.; Galli, G.; Wang, F. Emerging photoluminescence in monolayer MoS_2. *Nano Lett.* **2010**, *10*, 1271−1275.
(28) Liu, M.; Hisama, K.; Zheng, Y.; Maruyama, M.; Seo, S.; Anisimov, A.; Inoue, T.; Kauppinen, E. I.; Okada, S.; Chiashi, S.; Xiang, R.; Maruyama, S. Photoluminescence from Single-Walled MoS_2 Nanotubes Coaxially Grown on Boron Nitride Nanotubes. *ACS Nano* **2021**, *15*, 8418−8426.
(29) Margolin, A.; Rosentsveig, R.; Albu-Yaron, A.; Popovitz-Biro, R.; Tenne, R. Study of the Growth Mechanism of WS_2 Nanotubes Produced by a Fluidized Bed Reactor. *J. Mater. Chem.* **2004**, *14*, 617−624.
(30) Kern, W. The Evolution of Silicon Wafer Cleaning Technology. *J. Electrochem. Soc.* **1990**, *137*, 1887−1892.
(31) Yoshimoto, M.; Maeda, T.; Onihsi, T.; Koinuma, H.; Ishiyama, O.; Shinohara, M.; Kubo, M.; Miura, R.; Miyamoto, A. Atomic-scale formation of ultrasmooth surfaces on sapphire substrates for high-quality thin fin fabrication. *Appl. Phys. Lett.* **1995**, *67*, 2615−2617.
(32) Kresse, G.; Furthmu, J. Efficient iterative schemes for ab initio total-energy calculations using a plane-wave basis set. *Phys. Rev. B* **1996**, *54*, No. 11169.
(33) Perdew, J. P.; Ernzerhof, M.; Burke, K. Rationale for mixing exact exchange with density functional approximations. *J. Chem. Phys.* **1996**, *105*, 9982−9985.
(34) Srivastava, R.; Chase, L. L. Raman Spectra of CrO_2 and MoO_2 Single Crystals. *Solid State Comm.* **1972**, *11*, 349−353.
(35) Kumari, L.; Ma, Y.-R.; Tsai, C.-C.; Lin, Y.-W.; Wu, S. Y.; Cheng, K.-W.; Liou, Y. X-Ray Diffraction and Raman Scattering Studies on Large-Area Array and Nanobranched Structure of 1D MoO_2 Nanorods. *Nanotechnology* **2007**, *18*, No. 115717.
(36) Zhou, J.; Xu, N. S.; Deng, S. Z.; Chen, J.; She, J. C. Synthesis of large-scaled MoO_2 nanowire arrays. *Chem. Phys. Lett.* **2003**, *382*, 443−446.
(37) Scanlon, D. O.; Watson, G. W.; Payne, D. J.; Atkinson, G. R.; Egdell, R. G.; Law, D. S. L. Theoret-ical and Experimental Study of the Electronic Structures of MoO_3 and MoO_2. *J. Phys. Chem. C* **2010**, *114*, 4636−4645.
(38) Ahn, E.; Min, T.; Lee, J.; Lee, I.; Kim, Y.; Jeen, H. Role of surface oxidation for thickness-driven insulator-to-metal transition in epitaxial MoO_2 films. *Appl. Surf. Sci.* **2018**, *459*, 92−97.
(39) Dieterle, M.; Mestl, G. Raman Spectroscopy of Molybdenum Oxides Part I. Structural Characterization of Oxygen Defects in MoO3-x by DR UV/VIS, Raman Spectroscopy and X-ray Diffraction. *Phys. Chem. Chem. Phys.* **2002**, *4*, 822−826.
(40) Koma, A.; Sunouchi, K.; Miyajima, T. Fabrication of ultrathin heterostructures with van der Waals epitaxy. *J. Vac. Sci. Technol., B* **1985**, *3*, 724−725.
(41) Saiki, K.; Ueno, K.; Shimada, T.; A Koma, A. Application of van der Waals epitaxy to highly heterogeneous systems. *J. Cryst. Growth* **1989**, *95*, 603−606.
(42) Ueno, K.; Saiki, K.; Shimada, T.; Koma, A. Epitaxial Growth of Transition Metal Dichalcogenides on Cleaved Faces of Mica. *J. Vac. Sci. Technol., A* **1990**, *8*, 68−72.
(43) DeGregorio, Z. P.; Yoo, Y.; Johns, J. E. Aligned MoO_2/MoS_2 and $MoO_2/MoTe_2$ Freestanding Core/Shell Nanoplates Driven by Surface Interactions. *J. Phys. Chem. Lett.* **2017**, *8*, 1631−1636.
(44) Dahl-Petersen, C.; Saric, M.; Brorson, M.; Moses, P. G.; Rossmeisl, J.; Lauritsen, J. V.; Helveg, S. Topotactic Growth of Edge-Terminated MoS_2 from MoO_2 Nanocrystals. *ACS Nano* **2018**, *12*, 5351−5358.
(45) Lien, D. H.; Uddin, S. Z.; Yeh, M.; Amani, M.; Kim, H.; Ager, J. W., III; Yablonovitchi, E.; Javey, A. Electrical suppression of all nonradiative recombination pathways in monolayer semiconductor. *Science* **2019**, *364*, 468−471.
(46) Fathipour, S.; Remskar, M.; Varlec, A.; Ajoy, A.; Yan, R.; Vishwanath, S.; Rouvimov, S.; Hwang, W. S.; Xing, H. G.; Jena, D.; Seabaugh, A. Synthesized multiwall MoS_2 nanotube and nanoribbon field-effect transistors. *Appl. Phys. Lett.* **2015**, *106*, No. 022114.

https://doi.org/10.1021/acsomega.2c05586
ACS Omega 2022, 7, 39362−39369